nature communications

Article

https://doi.org/10.1038/s41467-024-55680-2

Sulfur-locked multiple resonance emitters for high performance orange-red/deep-red OLEDs

Received: 12 July 2024

Accepted: 19 December 2024

Published online: 02 January 2025

Check for updates

Yexuan Pu[1], Qian Jin[2], Yuewei Zhang[3,4] ✉, Chenglong Li[1] ✉, Lian Duan[2,3] ✉ & Yue Wang[1] ✉

Multiple resonance thermally activated delayed fluorescence (MR-TADF) materials are preferred for their high efficiency and high colour purity in organic light-emitting diodes (OLEDs). However, the design strategies of MR-TADF emitters in the red region are very limited. Herein, we propose a concept for a paradigm shift in orange-red/deep-red MR emitters by linking the outer phenyl groups in a classical MR framework through intramolecular sulfur (S) locks. Endowed with the planar architectural feature of the MR mother core, the proof-of-concept S-embedded emitters S-BN and 2S-BN also exhibit considerable flatness, which proves critical in avoiding the direct establishment of potent charge transfer states and inhibiting the non-radiative decay process. The emission maxima of S-BN and 2S-BN are 594 nm and 671 nm, respectively, and both have a high photoluminescence quantum yield of ~100%, a rapid radiative decay rate of around 10^7 s^{-1}, and a remarkably high reverse intersystem crossing rates of about 10^5 s^{-1}. Notably, maximum external quantum efficiencies of 39.9% (S-BN, orange-red) and 29.3% (2S-BN, deep-red) were also achieved in typical planar OLED structures with ameliorated efficiency roll-offs.

Orange-red/deep-red organic light-emitting diodes (OLEDs) have attracted considerable attention due to their potential applications in biomedical imaging[1], clinical practice[2], night vision[3], optical communications[4], and other fields[5,6]. Unfortunately, conventional flexible molecules are limited in their luminescence efficiency by the "loose bolt" and "free rotor" effects[7,8], resulting in relatively modest photoluminescence quantum yields (PLQYs). Consequently, strategies have been implemented that use perdeuterated/perfluorinated molecules to suppress the high-frequency vibrations associated with stretching of the C-H, O-H and N-H bonds, thereby mitigating the electronic-vibrational energy transfer within these models[9–11]. However, these methods face significant challenges in terms of synthesis, economic feasibility and practical effectiveness.

Instead, researchers have preferred to use rigid and fused polycyclic frameworks to construct long-wavelength (>580 nm) emitters that can effectively suppress the non-radiative decay mechanisms mentioned above[12–15]. While this strategy has been partially successful with red fluorescent and thermally activated delayed fluorescence (TADF) materials, it faces the challenge of a broader emission spectrum that is not well suited for the realization of future wide color gamut displays such as Ultra High Definition (UHD) TV. Despite the use of color filters and optical microcavities to reduce the full width at half maximum (FWHM) of the electroluminescence (EL) spectra in the latest OLEDs, the development of high-efficiency red emitters with narrowband emission is highly desired to realize displays with high color purity.

[1]State Key Laboratory of Supramolecular Structure and Materials, College of Chemistry, Jilin University, Changchun 130012, P. R. China. [2]Key Lab of Organic Optoelectronics and Molecular Engineering of Ministry of Education, Department of Chemistry, Tsinghua University, Beijing 100084, P. R. China. [3]Laboratory of Flexible Electronics Technology, Tsinghua University, Beijing 100084, P. R. China. [4]Applied Mechanics Lab, School of Aerospace Engineering, Tsinghua University, Beijing 100084, P. R. China. ✉e-mail: zhangyuewei@mail.tsinghua.edu.cn; chenglongli@jlu.edu.cn; duanl@mail.tsinghua.edu.cn; yuewang@jlu.edu.cn

Recently, the emergence of rigid polycyclic aromatic hydrocarbons characterized by multiple resonance (MR)[16–22] represents a promising avenue for the construction of high-performance and high color-purity emitters. The triumph of this methodology hinges on the incorporation of electron-donating and electron-withdrawing atoms with complementary resonance effects, which drastically localizes the frontier molecular orbitals (FMOs) on the atoms. The resulting non-bonding molecular orbitals (MOs) are capable of minimizing vibronic coupling and vibrational relaxation in the material, thereby significantly reducing the overlap of vibrational wave functions and structural displacements between the ground (S_0) and excited (S_1) states and avoiding non-radiative transitions. At the same time, MR offers other advantageous properties, such as narrowband emission, high absolute PLQY, and TADF, which have attracted considerable interest. For example, since the pioneering DABNA[23], numerous high-performance blue and green MR emitters have been unveiled[24–28], facilitating the fabrication of narrowband OLEDs with external quantum efficiencies (EQEs) surpassing 30% and small FWHMs < 25 nm.

Although MR materials with blue to green emissions have flourished, to our knowledge, their orange-red/deep-red potential needs to be further explored, an issue that needs to be addressed for further applications. On one hand, the development of most orange-red to deep-red MR molecules is bound within a double boron (B)-conjugated structure of para B-π-B[29–31], which faces constraints related to molecular backbone/synthesis methodology, low reaction yield, and substantial molecular mass, hindering commercialization (Fig. 1a). To our knowledge, no MR emitters with deep-red emission using a single boron atom have been disclosed. On the other hand, orange-red/deep-red MR OLEDs are often subject to significant efficiency roll-offs due to the constraints imposed by slow reverse intersystem crossing (RISC) rates, resulting in sub-par device performance at high brightness intensities (≥1000 cd m^{-2})[30,31].

To address the aforementioned challenges concurrently, we herein propose a concept for a paradigm shift in orange-red/deep-red MR emitters by incorporating additional electron-donating sulfur (S) locks into the highest occupied molecular orbital (HOMO) positions of a classical MR framework (BCz-BN[32,33]) (Fig. 1b). Based on the rigid structure of the BCz-BN mother core, the S-BN/2S-BN obtained by the introduction of the S-lock(s) also have considerable flatness, which proves crucial in avoiding the direct establishment of strong charge transfer (CT) states that undermine the MR molecule's inherent weak vibrational coupling and small structural displacement between the S_0 and S_1 states (i.e., promoting the non-radiative decay process). At the same time, the multiple ortho and para N-π-S structures contribute to the enhancement of the delocalized excited states of the molecule[34], resulting in a pronounced red shift of the luminescence spectrum, a decrease in the singlet-triplet (T_1) energy gap (ΔE_{ST}), and an acceleration of the RISC process. As intended, orange-red/deep-red emitters with peaks at 594 nm (S-BN) and 671 nm (2S-BN) were obtained, while exhibiting narrow FWHMs of 54 nm and high PLQYs of ~100% in toluene. To the best of our knowledge, 2S-BN was the first single-boron based deep-red MR dye. The significantly suppressed non-radiative transitions (~10^5 s^{-1}) and impressively high radiative decay rates of ~10^7 s^{-1} demonstrate the efficacy of this molecular architecture for the construction of highly efficient red emitters. Record-high maximum EQEs (EQE_{max}s) of 39.9% (S-BN, orange-red) and 29.3% (2S-BN, deep-red) were achieved in typical planar OLED structures with ameliorated efficiency roll-offs.

Results

Synthesis

The synthetic methodology of S-BNs is shown in Fig. 1b and Supplementary Fig. 1. The key precursor BCz-BN was prepared by a one-step lithiation-borylation reaction in two steps from commercially available sources. Subsequently, using 50 equivalents of sulfur as a reagent and 0.4 equivalents of iodine as a catalyst, the designated targets S-BN and 2S-BN were successfully obtained through a one-step synthesis method with impressive yields of 45% and 32%, respectively. It is noteworthy that, no palladium or alternative transition metal catalysts were used here, rendering it financially efficient. Consistent with classical MR materials, both S-BN and 2S-BN were soluble in common organic solvents (toluene, dichloromethane, tetrahydrofuran, etc.).

The structure of 2S-BN was further confirmed by X-ray crystallographic analysis (Fig. 1b and Supplementary Figs. 7–8). A notable

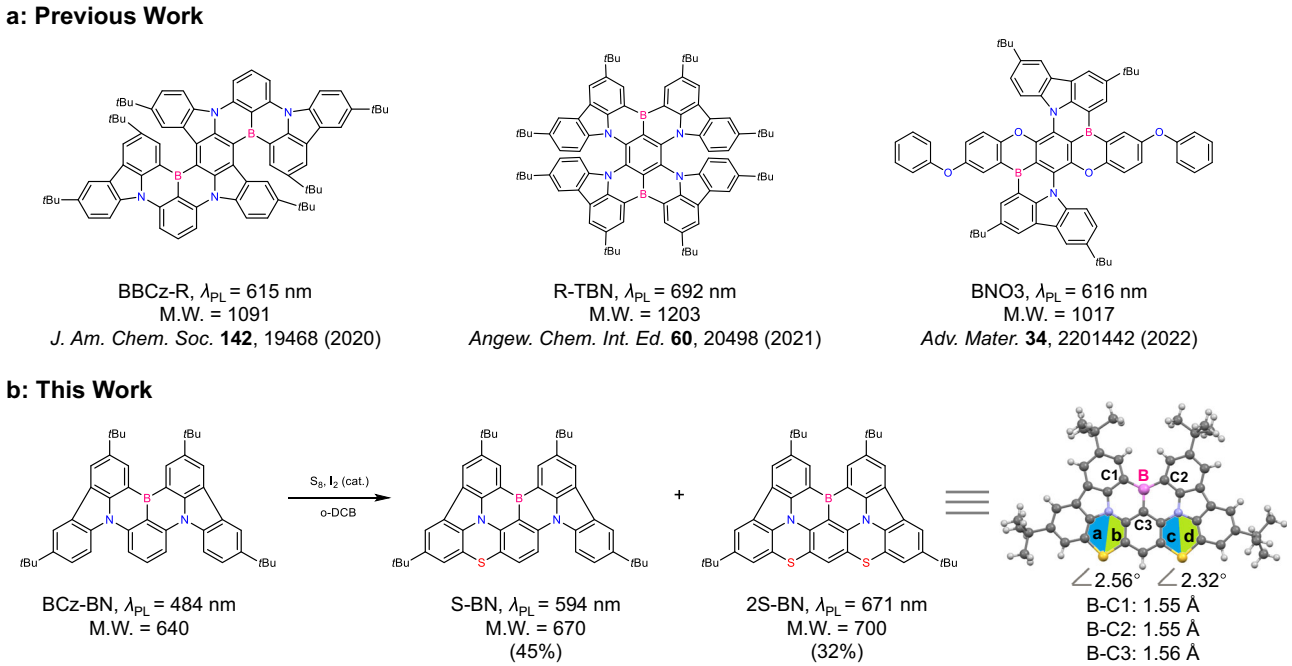

Fig. 1 | Representative orange-red/deep-red MR molecules. a The typical orange-red/deep-red MR molecules with para B-π-B structures. **b** Synthesis methods and molecular structures of S-BN and 2S-BN. Right: The crystal structure of 2S-BN.

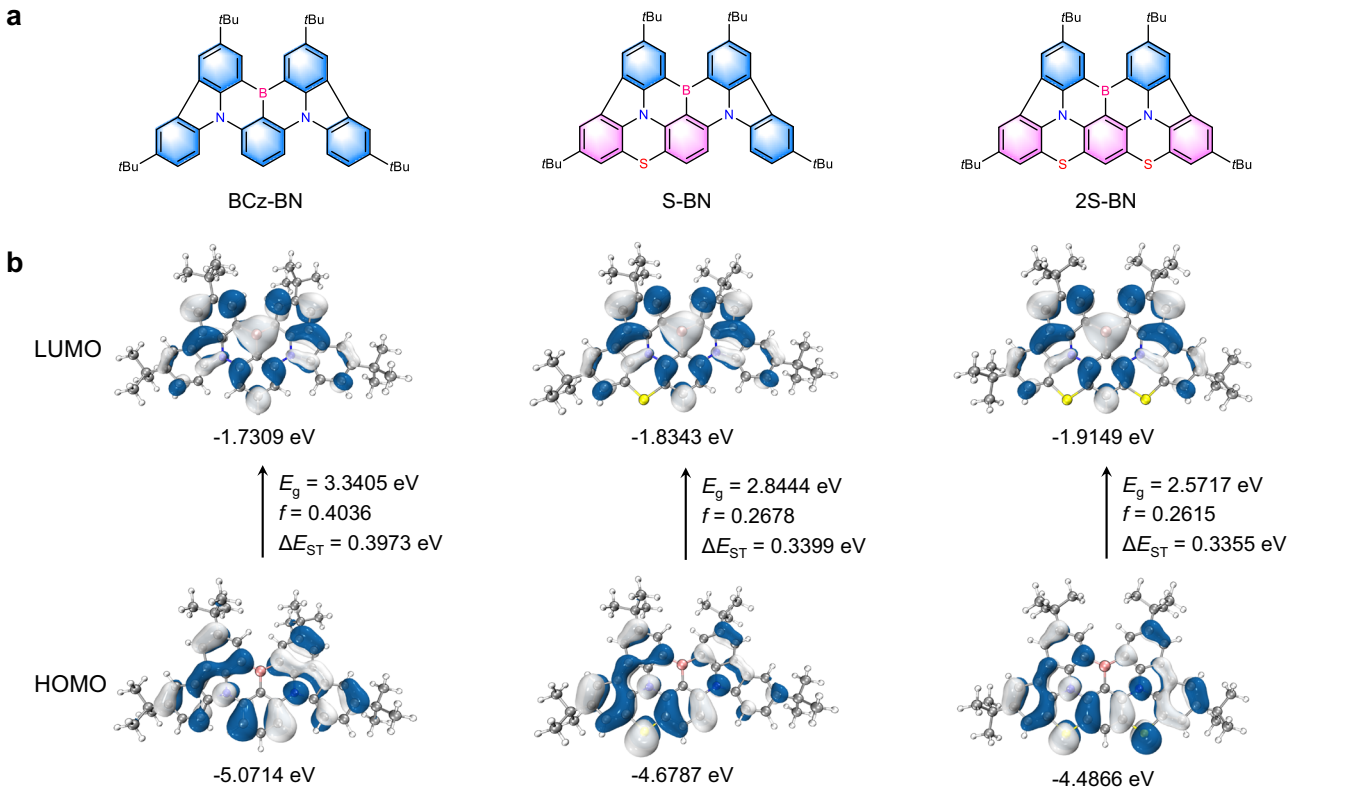

Fig. 2 | Theoretical analysis. a The chemical architectures of BCz-BN, S-BN and 2S-BN comprise multiple ortho and para N-π-S fragments. **b** The DFT-calculated HOMO and LUMO distributions, energy levels, energy gaps and oscillator strengths (*f*) of BCz-BN, S-BN and 2S-BN.

feature of this molecule is its remarkable planarity, which underlies its good luminescence performance in the deep-red spectrum. The dihedral angles encompassing the thioheterocyclic units are trivial values of only 2.56° (a-b) and 2.32° (c-d), respectively. The B-C bond lengths fall comfortably within the interval of 1.55-1.56 Å, cataphorically indicating the single bond nature. Consistent with conventional MR materials, robust intermolecular π-π stacking interactions exist between the backbones (contact length: 3.35 Å, overlap area: 80%). This interplay ultimately culminates in the formation of 2S-BN dimers.

Molecular design and theoretical calculations

To fully comprehend the implications of skeletal alterations on both the geometric and optoelectronic properties, density functional theory (DFT) and time-dependent DFT (TD-DFT) calculations were performed on the basis of the optimized structure (S-BN)/ single-crystal structure (2S-BN) at the B3LYP/6-31 G (d, p) level (Fig. 2). The benchmark compound, BCz-BN, an archetypal blue-green MR emitter with identical single-borylated framework as the study substances, served as a reference species. Based on the rigid structure of the BCz-BN mother core, the S-BN/2S-BN obtained by introducing the S-lock(s) also have substantial flatness (as illustrated in the 2S-BN crystal structure, Supplementary Figs. 7–9 and Table 1), a factor crucial for ensuring the target molecules mitigate the overlap of vibrational wave functions and structural displacements between the S_0 and S_1 whilst experiencing substantial red shifts.

For photophysical modulation, the pronounced redshift emissions originating from S-BNs are primarily enabled by the enhanced electron-donating capabilities induced by the multiple N-π-S motifs, synergistically combined with the positive conjugation effects induced by the extended π conjugation lengths (Fig. 2a). These effects could be elucidated by the enhancement and reduction of HOMO and the lowest unoccupied molecular orbital (LUMO) energy levels, respectively (Fig. 2b and Supplementary Table 2). Furthermore, these new paradigms also provided convenience in achieving smaller ΔE_{ST} values while maintaining high oscillator strengths (*f*s), an essential prerequisite for fabricating high-performance orange-red and deep-red emitters with elevated PLQYs and rapid RISC rates (k_{RISC}s) (Fig. 2b and Supplementary Table 2).

In terms of inhibiting the non-radiative decay process, S-BN/2S-BN could significantly reduce the probability of S_1-S_0 internal conversion (IC) compared to conventional acceptor-donor type TADF red emitters[14,15]. Reorganization energy and RMSD calculations indicate that S-BN/2S-BN has very little structural changes in ground and excited state structures (Supplementary Figs. 11–13). Consequently, it can be assumed that there is no zero level crossing between its ground and excited states. Under these circumstances, the S_1-S_0 internal transition (non-radial jump) has to occur through the Franck-Condon forbidden mechanisms[35]. According to the distribution of FMOs, the non-bonding characteristics of the BCz-BN core could be preserved in the S-BN/2S-BN, that is the highest occupied molecular orbitals (HOMOs) predominantly profiled on the N/S atoms and the carbon atoms at their ortho/para positions, while the lowest unoccupied molecular orbitals (LUMOs) were primarily situated on the B atoms and the carbon atoms at their ortho/para positions. This so-called non-bonding character could significantly lower the vibration frequency in the molecules, thereby making it difficult to establish an efficient wave function overlap with the elevated vibrational energy level of the ground state, culminating in a significant reduction in the likelihood of the occurrence of nonradiative decays.

Photophysical properties

The photophysical properties of these emitters were analyzed in a dilute toluene solution (1×10^{-5} M), and the results were presented in Fig. 3 and Table 1. Both S-BNs displayed archetypal MR absorption characteristics, including elaborate absorption bands within the spectral range of 300–500 nm and sharp absorption peaks beyond

https://doi.org/10.1038/s41467-024-55680-2

Table 1 | The physical data of BCz-BN, S-BN and 2S-BN

Emitter	λ_{abs} [nm]	λ_{em} [nm]	FWHM[a] [nm/eV]	E_{S1} [eV]	E_{T1} [eV]	ΔE_{ST} [eV]	PLQY[d] [%]	τ_p [ns]	Ref_p [%]	τ_d [μs]	Ref_d [%]	k_r (10^7 s^{-1})	k_{nr} (10^5 s^{-1})	k_{RISC} (10^5 s^{-1})
BCz-BN	467	484	25/0.12	2.66	2.46	0.20	91.0	6.70	63.6	56.7	36.4	8.64	85.4	0.28
S-BN	553	594	54/0.18	2.22	2.13	0.09	99.2	9.24	40.6	15.30	50.4	4.35	3.51	1.61
2S-BN	629	671	54/0.15	1.96	1.90	0.06	98.4	10.68	35.9	7.63	64.1	3.30	5.37	3.66

[a]Measured in dilute toluene solution at 300 K.
[b]Measured in dilute toluene solution at 77 K.
[c]S_1-T_1 energy gap.
[d]Measured in dilute toluene solution after N_2 bubbling for 10 min at 300 K.

500 nm, attributed to π-π* and short-range charge transfer (SR-CT) transitions, respectively (Fig. 3a and Supplementary Fig. 17). As a result of the enhanced electron-donating capabilities and extended π-conjugations, S-BN and 2S-BN revealed orange-red and deep-red luminescence at 594 nm and 671 nm, respectively, with significant red shifts of over 110 nm/474 meV and 187 nm/714 meV compared to the original BCz-BN core (emission maximum: 484 nm) (Fig. 3a). To our knowledge, S-BNs were the simplest structured orange-red/deep-red MR emitters available[29–31]. At the same time, 2S-BN was the first single boron based deep-red MR material, highlighting the sophistication of this molecular design methodology[29–31]. The Stokes shifts and FWHM values were calculated to be 41 nm/155 meV and 54 nm/184 meV for S-BN, 42 nm/123 meV and 54 nm/149 meV for 2S-BN, respectively, demonstrating that the molecular vibrational coupling and relaxation were suppressed. Taking advantage of the weak vibrational coupling and minute structural displacement between the S_0 and S_1 states of MR configurations, S-BNs manifested remarkably high PLQY values, close to 100%. Such achievements symbolize a significant suppression of non-radiative decay pathways, correcting the recognized limitations of the energy gap paradigm outlined above.

The ΔE_{ST} values, calculated from the onset of the fluorescence and phosphorescence (77 K in toluene) spectra, were 0.09 eV for S-BN and 0.06 eV for 2S-BN (Fig. 3b). These small values facilitated the TADF at ambient conditions, which could be verified by temperature-dependent transient photoluminescence (PL) decay experiments (Fig. 3d). The prompt (τ_{PF}) and delayed (τ_{DF}) lifetimes at room-temperature deoxygenated solutions were measured to be 9.24 ns and 15.30 μs for S-BN and 10.68 ns and 7.63 μs for 2S-BN, respectively (Fig. 3c and Supplementary Figs. 18–19). Following by a classical methodology[36], the rate constants of radiative decays (k_rs), inter-system crossings (k_{ISC}s), RISCs (k_{RISC}s) and non-radiative transitions (k_{nr}s) were subsequently determined to be $4.35 \times 10^7\,s^{-1}$, $6.43 \times 10^7\,s^{-1}$, $1.61 \times 10^5\,s^{-1}$, and $3.51 \times 10^5\,s^{-1}$ for S-BN, $3.30 \times 10^7\,s^{-1}$, $5.99 \times 10^7\,s^{-1}$, $3.66 \times 10^5\,s^{-1}$, and $5.37 \times 10^5\,s^{-1}$ for 2S-BN respectively. In contrast to previously reported BCz-BN structures, which generally exhibit sustained lifetimes of several hundred microseconds or even milliseconds and k_{RISC}s of 10^2 ~ $10^4\,s^{-1}$(refs. 28,37), the S-BNs exhibited significantly shortened delayed lifetimes and accelerated RISC rates, as indicated by their smaller ΔE_{ST} values. This property is favored in EL due to the greater likelihood that upconverted triplet excitons will emit light via the RISC mechanism, bypassing deleterious spin-flip cycles and avoiding energy loss[38].

Electroluminescent performance

Given the exceptional photophysical properties of these orange-red/deep-red emitters, their potential for EL performance in devices was then thoroughly investigated. The OLEDs were fabricated using the following optimized architecture: ITO/ 4,4′-cyclohexylidenebis[N,N-bis(4-methylphenyl)benzenamine] (TAPC, 50 nm)/ tris(4-(9H-carbazol-9-yl)phenyl)amine (TCTA, 10 nm)/ the emitting layer (30 nm)/ 1,3,5-tri[(3-pyridyl)-phen-3-yl]benzene (TmPyPb, 30 nm)/ lithium fluoride (LiF, 1 nm)/ Al (100 nm). LiF was used as the electron injection layer, TAPC and TmPyPb as the hole and electron transport layers, and TCTA as the electron blocking layer. For the emitting layer, DMIC-TRZ (1,3-dihydro-1,1-dimethyl-3-(3-(4,6-diphenyl-1,3,5-triazin-2-yl)phenyl) indeno-[2,1-b]carbazole) was chosen as the host due to its suitable HOMO/LUMO energy levels and balanced charge injection and transport capabilities[39], with the dopant concentration level optimized at 0.5 wt%. The energy level diagram of the devices as well as the molecular structures of the materials used in the organic layers are shown in Fig. 4a and Supplementary Fig. 21.

As shown in Fig. 4b, Supplementary Figs. 22–23 and Supplementary Tables 3–4, these OLEDs exhibited bright orange-red and deep-red emissions with peaks, FWHMs and CIE coordinates of 600 nm, 58 nm/198 meV and (0.61, 0.39) for S-BN and 676 nm, 62 nm/164 meV and

https://doi.org/10.1038/s41467-024-55680-2

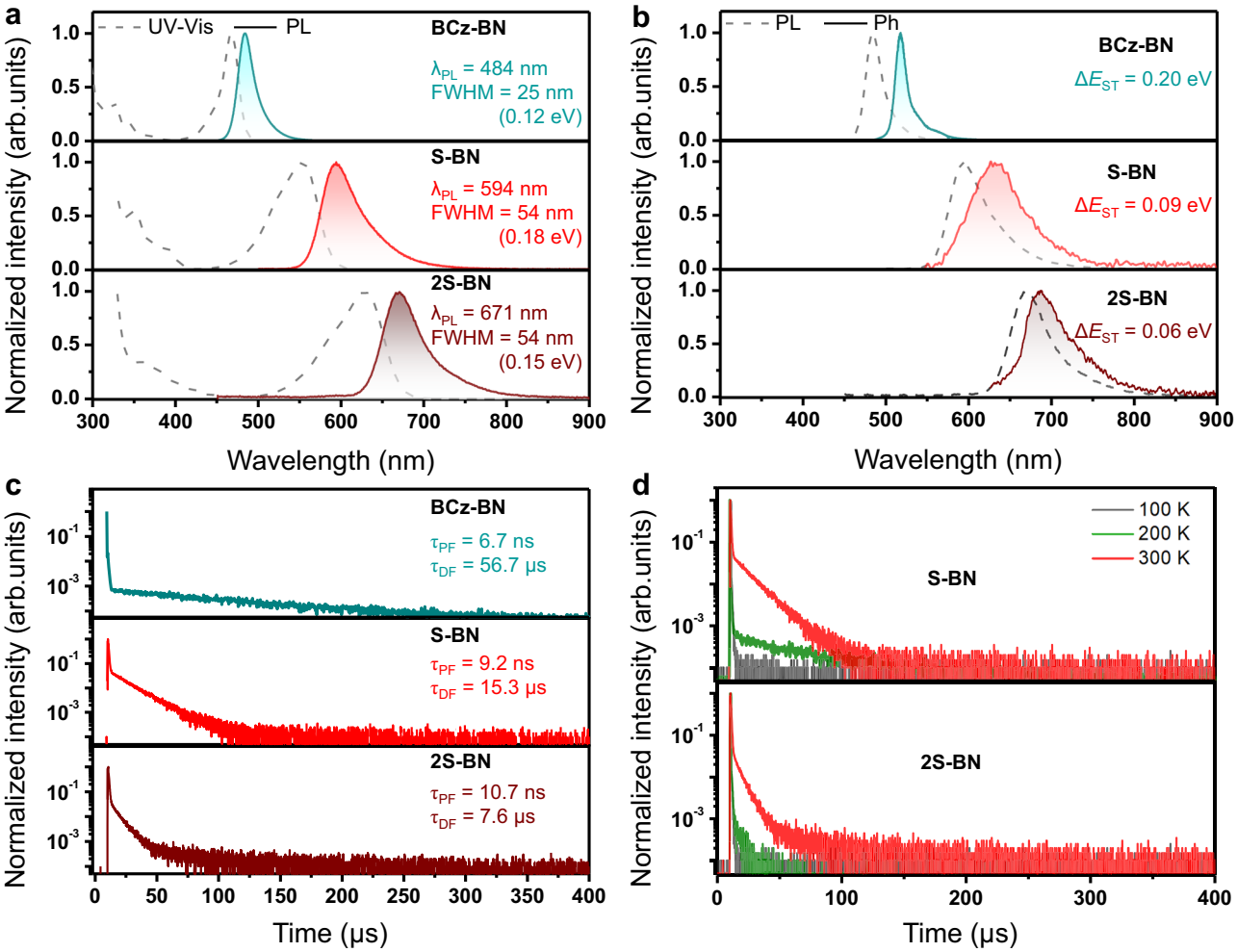

Fig. 3 | Photophysical properties of BCz-BN, S-BN, and 2S-BN. a Ultraviolet-visible (UV-vis) absorption and fluorescence spectra at 300 K in toluene (1×10^{-5} M). **b** Normalized fluorescence at 300 K and phosphorescence spectra at 77 K of the emitters in toluene (1×10^{-5} M), where ΔE_{ST} denotes the energy gap between the lowest singlet and triplet excited states. **c** Transient photoluminescence decay curves in toluene after N_2 bubbling for 10 min, where τ_{PF} and τ_{DF} denote the prompt and delayed fluorescence lifetimes, respectively. **d** Transient photoluminescence decay curves at various temperatures.

(0.70, 0.28) for 2S-BN, respectively. Among them, the 2S-BN-based OLED can experience a remarkable redshift of >190 nm/717 meV when contrasted with the BCz-BN parent core, marking the first single-boron deep-red MR-OLED. As for the slightly broadened EL spectra (compared to the PL spectra in dilute solutions), these can be attributed to the potential host-dopant and dopant-dopant interactions resulting from the planar configurations. In addition to the noticeable spectral redshifts, the devices also exhibited considerable EQE_{max}s of 39.9% (S-BN) and 29.3% (2S-BN), which visibly result from the high PLQY and horizontal dipole ratio (Θ//) values of the S-BNs, highlighting the effectiveness of the aforementioned molecular design methodology (Fig. 4c and Supplementary Fig. 24). To the best of our knowledge, these efficiencies surpassed those of orange-red and deep-red MR-OLEDs[40–64], respectively (Fig. 4d, Supplementary Fig. 26 and Supplementary Table 5), and were indeed paralleled by the high-efficiency TADF devices with similar emission maxima[10]. Taking advantage of the relatively fast k_{RISC}s, the efficiency roll-offs of these devices were substantially ameliorated. At a brightness of 1000 cd m^{-2}, the EQE values of these devices remained at substantial levels of 26.3% and 16.7%, which were the highest values for orange-red (S-BN) and deep-red (2S-BN) MR-OLEDs, respectively, at this luminance (Fig. 4d and Supplementary Table 5). To validate the high EQE values, we also measured the angle-dependent EL intensities of the devices based on S-BN and 2S-BN, and nearly Lambertian profile patterns with Lambertian coefficients of 0.98 (S-BN) and 0.99 (2S-BN) were recorded (Supplementary Fig. 31). The EQE_{max}s of the S-BNs devices were recalculated by Lambertian calibration to be still up to 39.1% (S-BN) and 29.0% (2S-BN), indicating that the high device efficiencies were not overstimated.

To further improve the performance of the aforementioned devices and to suppress the efficiency roll-off, a sensitization strategy was employed[65] (Fig. 5a, Supplementary Figs. 27–30 and Supplementary Tables 6-7). The remarkable phosphorescent emitters bis(4-phenyl-thieno[3,2-c]pyridinato-C2,N)(acetylacetonato)iridium(III) (PO-01) and bis(1-phenyl-isoquinoline)(acetylacetonato)iridium(III) ($Ir(piq)_2acac$) were chosen as sensitizers[66,67], taking advantage of their well-matched PL spectra with the absorption spectra of S-BNs, high PLQYs and short excited state lifetimes. As shown in Supplementary Fig. 28, substantial spectral overlap between the absorption and emission spectra was achieved, along with large Förster energy transfer (FET) radii of 5.28 Å for S-BN and 2.60 Å for 2S-BN, respectively, indicating remarkable FET efficiencies from the phosphorescent sensitizers to the MR emitters. The electroluminescence spectra of the S-BN and 2S-BN sensitized devices are identical to those of their non-sensitized ones, with corresponding peak wavelengths and FWHMs of 600 and 61 nm/205 meV, and 680 and 62 nm/166 meV, respectively (Fig. 5b). This indicates that energy is efficiently transferred from the sensitizers to the terminal emitters.

https://doi.org/10.1038/s41467-024-55680-2

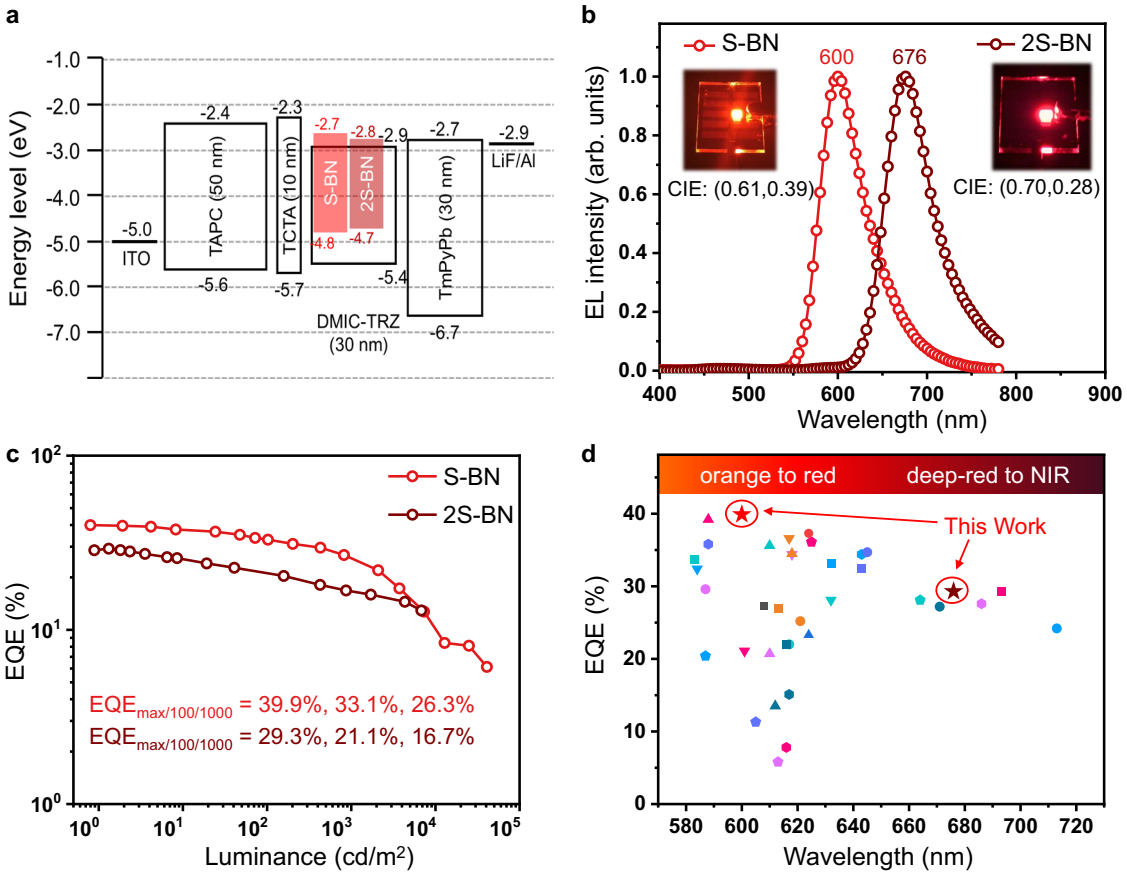

Fig. 4 | The electroluminescence performance of the non-sensitized OLEDs based on S-BN and 2S-BN. a Device architecture with energy level alignment of the relevant materials. **b** Electroluminescence spectra. Inset: EL images of the devices. **c** External quantum efficiency versus luminance (EQE – *L*) curves. **d** EQE versus wavelength plots of representative orange-red/deep-red MR-OLEDs without light-outcoupling enhancement techniques.

The EQE$_{max}$s of the sensitized devices reached 36.8% (S-BN) and 28.2% (2S-BN), again in the range of the highest values currently available for orange-red and deep-red MR-OLEDs[40–64], respectively (Figs. 4d, 5c and Supplementary Table 5).

It is noteworthy that at the elevated brightness level of 1000 cd m^{-2}, the EQEs remain at 34.6% and 20.9% and decrease only slightly by 6.0% and 25.9%, respectively, relative to the maximum efficiency, representing one of the best performances for orange-red and deep-red MR-OLEDs at this luminance (Fig. 5c and Supplementary Table 5). A substantial part of the remarkably suppressed efficiency roll-offs can be attributed to the relatively fast k_{RISC}s of S-BN and 2S-BN, which could accelerate the radiative dissipation of excitons to mitigate the potential exciton annihilations[68,69]. Regarding the relatively modest EQE$_{max}$s in sensitized devices, this could be attributed to the Dexter energy transfer dissipation pathway from the high energy T_1 of the sensitizers to the low energy T_1 of the target emitters[70]. By further introducing the steric wrapping groups to mitigate the direct interactions between the active molecules (host-dopant and dopant-dopant), the device performance can be further enhanced for the effectively suppressed DET[71,72]. In addition, the EL operating stability of phosphorescent-sensitized devices under constant current density with an initial luminance of 1000 cd/m^2 was also evaluated. The LT85s (lifetime to 85% of the initial luminance) of ~170 and ~320 h were obtained for S-BN and 2S-BN, respectively (Supplementary Fig. 32).

Discussion

In summary, we propose here a concept for a paradigm shift in orange-red/deep-red MR emitters by incorporating additional electron-donating sulfur (S) locks into the HOMO positions of a classical MR framework. The multiple ortho and para N-π-S structures contribute to the enhancement of the delocalized excited states of the molecule, resulting in a remarkable red shift of the luminescence spectrum, a reduction of the ΔE_{ST} value, and an enhancement of the RISC process. It is of greater significance that the proof-of-concept S-embedded emitters are capable of maintaining a high degree of flatness as a consequence of the planar architectural feature of the MR mother core. This is of paramount importance in preventing the direct formation of potent charge transfer states and inhibiting the non-radiative decay process. As expected, orange-red/deep-red emitters with peaks at 594 nm (S-BN) and 671 nm (2S-BN) were achieved while exhibiting high PLQYs of ~100%, significantly suppressed non-radiative transitions of ~10^5 s^{-1}, and impressively fast radiative decay rates of ~10^7 s^{-1}. Furthermore, narrowband orange-red/deep-red OLEDs based on these emitters with the phosphor sensitizer exhibited record-high EQEs of up to 36.8% (orange-red) and 28.2% (deep-red) with low efficiency roll-offs. We're confident that this strategic design approach will greatly accelerate the development of high-performance long-wavelength MR emitters and OLEDs.

Methods

Material

All reagents were purchased from commercial sources and used without further purification. ^{1}H NMR and ^{13}C NMR spectra were recorded on a Bruker 500/151 MHz spectrometer in deuterium reagent at room temperature. MALDI-TOF mass data were recorded on a Bruker ultrafleXtreme instrument.

https://doi.org/10.1038/s41467-024-55680-2

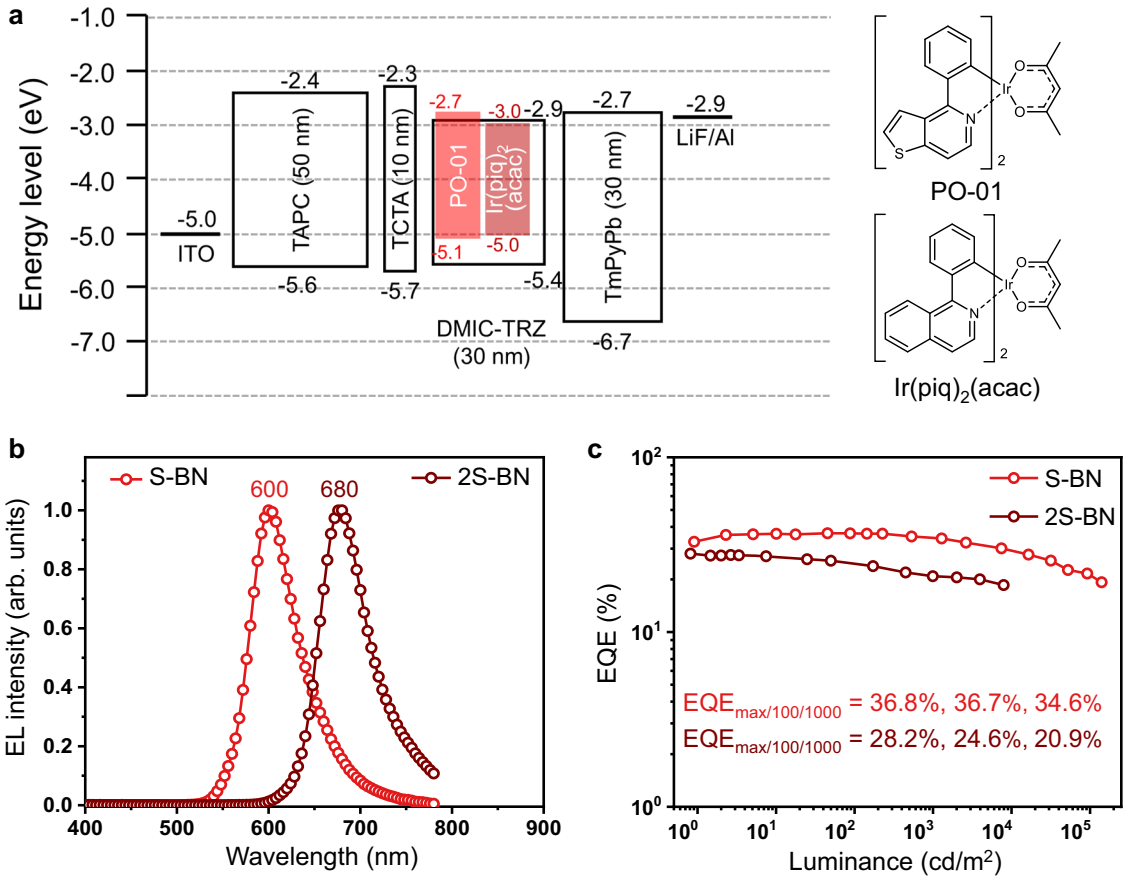

Fig. 5 | The electroluminescence performance of the phosphorescence sensitized OLEDs based on S-BN and 2S-BN. a Device architecture with energy level alignment of the relevant materials. **b** Electroluminescence spectra. **c** External quantum efficiency versus luminance (EQE − *L*) curves.

Computational methods

The calculations were performed using the Gaussian 16 package[73], employing the density functional theory (DFT) and time-dependent density functional theory (TD-DFT) methods. The B3LYP functionals were utilized[74–77]. The structures were optimized using DFT for S_0 state and TD-DFT for S_1 and T_1 states with a 6–31 G (d, p) basis set. The MOMAP software package was used to calculate the absorption and emission spectra and analyze the vibrational modes in the emission spectrum[78–81]. NTO analysis was performed using the Multiwfn package[82]. The spin-orbit coupling matrix elements (SOCEMs) between two first singlet and triplet excited states were calculated in B3LYP/6-31 G (d, p) level using Orca 4.2.1 package[83–85].

Measurement of absorption and emission characteristics

1×10^{-5} M solutions were prepared by stepwise dilution for solution measurements. UV-vis absorption spectra were measured using UV-2600 (Shimadzu) instrument. Photoluminescence (PL) spectra were recorded on FluoroMax-4P (Horiba) instrument and Hitachi F-4600 fluorescence spectrophotometer. The PLQYs were obtained with an absolute photoluminescence quantum yield measurement system Hamamatsu C9920-03G in an integrating sphere. The solution sample was bubbled with nitrogen for 10 min before measurement. The transient spectra were collected on an Edinburgh Fluorescence Spectroscopy FLS1000.

Thermal characterization

In the range of 25–800 °C, TA Q500 thermogravimeter was selected to perform the thermogravimetric analysis (TGA) of target molecules under nitrogen atmosphere at a heating rate of 10 K min^{-1}. The decomposition temperatures (T_d) of the compounds were measured at 5% weight loss. The T_d values of the S-BN and 2S-BN were 435 °C and 465 °C.

Electrochemical characterization

BAS 100 W Bioanalytical electrochemical work station was used to measure the electrochemical property with platinum disk as working electrode, platinum wire as auxiliary electrode, a porous glass wick Ag/Ag^+ as pseudo reference electrode and ferrocene/ferrocenium as the internal standard. And 0.1 M solution of n-Bu_4NPF_6 which was the supporting electrolyte was utilized to measure the reduction (in anhydrous tetrahydrofuran) potentials with a scan rate of 100 mV s^{-1}. The oxidation potentials were calculated from E_{red} and E_g, the optical bandgaps (E_g) were estimated from the onset of the absorption spectra.

Determination of the emitting dipole orientation

To determine emitting dipole orientation of an emitting film, angle-resolved and polarization-resolved PL measurements were performed by Hamamatsu's established molecular orientation measurement system (C14234-11, Hamamatsu Photonics). The sample consisted of a fused silica substrate with a 10 nm-thick film doped with emitters. Thin films for photophysical characterization were prepared by thermal evaporation on quartz substrates at 1–2 Å s^{-1} in a vacuum chamber with a base pressure of <10^{-5} torr. The sample was attached to a fused silica half-cylinder prism by index matching liquid. The excitation of the samples was performed with the 360 nm line of the continuous-wave laser with a fixed excitation angle of 45°. The angle-dependent p-polarized emission intensity at the peak wavelength of the PL spectrum of the emitting layer was detected. The emitting dipole orientation was

then determined by least-square fitting of the measured angle-dependent polarized emission intensity with calculated results.

Device fabrication and measurement of EL characteristics

All compounds were subjected to temperature-gradient sublimation under a high vacuum before use. OLEDs were fabricated on the ITO-coated glass substrates with multiple organic layers sandwiched between the transparent bottom indium-tin-oxide (ITO) anode and the top metal cathode. Before device fabrication, the ITO glass substrates were pre-cleaned carefully. All material layers were deposited by vacuum evaporation in a vacuum chamber with a base pressure of 10^{-6} torr. The deposition system permits the fabrication of the complete device structure in a single vacuum pump-down without breaking the vacuum. The deposition rate of organic layers was kept at 0.1 ~ 0.2 nm s^{-1}. The doping was conducted by co-evaporation from separate evaporation sources with different evaporation rates. The EL spectrum, CIE coordinates and luminance intensity of OLEDs were recorded by Photo Research PR655, meanwhile, the current density (*J*) and driving voltage (*V*) were recorded by Keithley 2400. By assuming Lambertian distribution, EQE was estimated according to brightness, electroluminescence spectrum and current density.

Data availability

The data supporting the findings of this study are available within the paper and the Supplementary Information. Crystallographic data for the structure reported in this Article have been deposited at the Cambridge Crystallographic Data Centre, under deposition number CCDC 2352386 (2S-BN). Copies of the data can be obtained free of charge via https://www.ccdc.cam.ac.uk/structures/. Source data are provided with this paper.

References

1. Hong, G., Antaris, A. & Dai, H. Near-infrared fluorophores for biomedical imaging. *Nat. Biomed. Eng.* **1**, 0010 (2017).
2. Jeon, Y. et al. Sandwich-structure transferable free-form OLEDs for wearable and disposable skin wound photomedicine. *Light Sci. Appl* **8**, 114 (2019).
3. Borek, C. et al. Highly efficient, near-infrared electrophosphorescence from a Pt–metalloporphyrin complex. *Angew. Chem. Int. Ed.* **46**, 1109–1112 (2007).
4. Tessler, N. et al. Efficient near-infrared polymer nanocrystal light-emitting diodes. *Science* **295**, 1506–1508 (2002).
5. Ho, C.-L., Li, H. & Wong, W.-Y. Red to near-infrared organometallic phosphorescent dyes for OLED applications. *J. Organomet. Chem.* **751**, 261–285 (2014).
6. Wu, X. et al. Multiple enol-keto isomerization and excited-state unidirectional intramolecular proton transfer generate intense, narrowband red OLEDs. *J. Am. Chem. Soc.* **146**, 24526–24536 (2024).
7. Rodrigues, A. C. B. & Seixas de Melo, J. S. Aggregation-induced emission: from small molecules to polymers-historical background, mechanisms and photophysics. *Top. Curr. Chem.* **379**, 15 (2021).
8. Wang, D. et al. D-A-type molecules with free rotors for highly efficient interfacial solar-driven steam generation and thermoelectric performance. *Org. Lett.* **25**, 5730–5734 (2023).
9. Huang, T. et al. Enhancing the efficiency and stability of blue thermally activated delayed fluorescence emitters by perdeuteration. *Nat. Photon* **18**, 516–523 (2024).
10. Ly, K. T. et al. Near-infrared organic light-emitting diodes with very high external quantum efficiency and radiance. *Nat. Photon* **11**, 63–68 (2017).
11. Wei, Y. C. et al. Overcoming the energy gap law in near-infrared OLEDs by exciton–vibration decoupling. *Nat. Photon* **14**, 570–577 (2020).
12. Chen, J.-X. et al. Red/Near-infrared thermally activated delayed fluorescence OLEDs with near 100% internal quantum efficiency. *Angew. Chem. Int. Ed.* **58**, 14660–14665 (2019).
13. Zhang, Y. et al. Rigid bridge-confined double-decker Platinum(II) complexes towards high-performance red and near-infrared electroluminescence. *Angew. Chem. Int. Ed.* **61**, e202113718 (2022).
14. Karthik, D. et al. Acceptor-donor-acceptor-type orange-red thermally activated delayed fluorescence materials realizing external quantum efficiency over 30% with low efficiency roll-off. *Adv. Mater.* **33**, e2007724 (2021).
15. Maeng, J. H. et al. Efficiency enhancement in orange red thermally activated delayed fluorescence OLEDs by using a rigid di-indolocarbazole donor moiety. *Dyes Pigments* **194**, 109580 (2021).
16. Yasuhiro, K. et al. Narrowband deep-blue organic light-emitting diode featuring an organoboron-based emitter. *Nat. Photon* **13**, 678–682 (2019).
17. Wu, X. et al. Fabrication of circularly polarized MR-TADF emitters with asymmetrical peripheral-lock enhancing helical B/N-doped nanographenes. *Adv. Mater.* **34**, 2105080 (2022).
18. Park, I. S. et al. Ultrafast triplet–singlet exciton interconversion in narrowband blue organoboron emitters doped with heavy chalcogens. *Angew. Chem. Int. Ed.* **61**, e202205684 (2022).
19. Xu, Y. et al. Constructing charge-transfer excited states based on frontier molecular orbital engineering: narrowband green electroluminescence with high color purity and efficiency. *Angew. Chem. Int. Ed.* **59**, 17442 (2020).
20. Wu, X. et al. The role of host–guest interactions in organic emitters employing MR-TADF. *Nat. Photon* **15**, 780–786 (2021).
21. Hu, Y. X. et al. Efficient selenium-integrated TADF OLEDs with reduced roll-off. *Nat. Photon* **16**, 803–810 (2022).
22. Fan, X.-C. et al. Ultrapure green organic light-emitting diodes based on highly distorted fused π-conjugated molecular design. *Nat. Photon* **17**, 280–285 (2023).
23. Hatakeyama, T. et al. Ultrapure blue thermally activated delayed fluorescence molecules: efficient HOMO–LUMO separation by the multiple resonance effect. *Adv. Mater.* **28**, 2777–2781 (2016).
24. Chan, C.-Y. et al. Stable pure-blue hyperfluorescence organic light-emitting diodes with high-efficiency and narrow emission. *Nat. Photon* **15**, 203–207 (2021).
25. Jeon, S. O. et al. High-efficiency, long-lifetime deep-blue organic light-emitting diodes. *Nat. Photon* **15**, 208–215 (2021).
26. Naveen, K. R. et al. Achieving high efficiency and pure blue color in hyperfluorescence organic light emitting diodes using organoboron based emitters. *Adv. Funct. Mater.* **32**, 2110356 (2022).
27. Suresh, S. M. et al. Multiresonant thermally activated delayed fluorescence emitters based on heteroatom-doped nanographenes: recent advances and prospects for organic light-emitting diodes. *Adv. Funct. Mater.* **30**, 1908677 (2020).
28. Mamada, M. et al. Organoboron-based multiple-resonance emitters: synthesis, structure–property correlations, and prospects. *Chem. Soc. Rev.* **53**, 1624–1692 (2024).
29. Fan, X. et al. RGB thermally activated delayed fluorescence emitters for organic light-emitting diodes toward realizing the BT.2020 standard. *Adv. Sci.* **10**, 2303504 (2023).
30. Naveen, K. R., Yang, H. I. & Kwon, J. H. Double boron-embedded multiresonant thermally activated delayed fluorescent materials for organic light-emitting diodes. *Commun. Chem.* **5**, 149 (2022).
31. Keerthika, P. & Konidena, R. K. Marching toward long-wavelength narrowband emissive multi-resonance delayed fluorescence emitters for organic light emitting diodes. *Adv. Opt. Mater.* **11**, 2301732 (2023).
32. Xu, Y. et al. Molecular-structure and device-configuration optimizations toward highly efficient green electroluminescence with narrowband emission and high color purity. *Adv. Opt. Mater.* **8**, 1902142 (2020).

33. Zhang, Y. et al. Multi-resonance induced thermally activated delayed fluorophores for narrowband green OLEDs. *Angew. Chem. Int. Ed.* **58**, 16912–16917 (2019).
34. Noda, H. et al. Critical role of intermediate electronic states for spin-flip processes in charge-transfer-type organic molecules with multiple donors and acceptors. *Nat. Mater.* **18**, 1084–1090 (2019).
35. Turro, N. J. et al. *Modern Molecular Photochemistry*, Vol. 1084 (Univ Science Books, 2015).
36. Wada, Y. et al. Organic light emitters exhibiting very fast reverse intersystem crossing. *Nat. Photon* **14**, 643–649 (2020).
37. Luo, X.-F., Xiao, X. & Zheng, Y.-X. Recent progress in multi-resonance thermally activated delayed fluorescence emitters with an efficient reverse intersystem crossing process. *Chem. Commun.* **60**, 1089–1099 (2024).
38. Zysman-Colman, E. Molecular designs offer fast exciton conversion. *Nat. Photon* **14**, 593–594 (2020).
39. Lv, X. et al. Blue TADF emitters based on indenocarbazole derivatives with high photoluminescence and electroluminescence efficiencies. *ACS Appl. Mater. Interfaces* **11**, 10758–10767 (2019).
40. Liu, Y. et al. Molecular design of thermally activated delayed fluorescent emitters for narrowband orange-red OLEDs boosted by a cyano-functionalization strategy. *Chem. Sci.* **12**, 9408–9412 (2021).
41. Yang, W. et al. An effective approach toward yellow-to-orange multi-resonance TADF emitters by integrating strong electron donor into B/N-based polycyclic architecture: high performance oleds with nearly 40% EQE. *Adv. Funct. Mater.* **33**, 2213056 (2023).
42. Du, M. et al. Stereo effects for efficient synthesis of orange-red multiple resonance emitters centered on a pyridine ring. *Chem. Sci.* **15**, 3148–3154 (2024).
43. Cai, X. et al. Precisely regulation of peripheral decoration of multi-resonance molecules and construction of highly efficient solution-processed orange-red OLEDs with external quantum efficiency approaching 20%. *Adv. Opt. Mater.* **12**, 2302811 (2024).
44. Cheng, Y.-C. et al. A highly twisted carbazole-fused DABNA derivative as an orange-red TADF emitter for OLEDs with nearly 40 % EQE. *Angew. Chem. Int. Ed.* **61**, e202212575 (2022).
45. Fan, X.-C. et al. A quadruple-borylated multiple-resonance emitter with para/meta heteroatomic patterns for narrowband orange-red emission. *Angew. Chem. Int. Ed.* **62**, e202305580 (2023).
46. Naveen, K. R. et al. Narrow band red emission fluorophore with reasonable multiple resonance effect. *Adv. Electron. Mater.* **8**, 2101114 (2022).
47. Chen, H. et al. Clar's aromatic π-sextet rule for the construction of red multiple resonance emitter. *Angew. Chem. Int. Ed.* https://doi.org/10.1002/anie.202415400 (2024).
48. Chen, H. et al. A simple molecular design strategy for pure-red multiple resonance emitters. *Angew. Chem. Int. Ed.* **62**, e202300934 (2023).
49. Cai, X. et al. Solution-processable pure-red multiple resonance-induced thermally activated delayed fluorescence emitter for organic light-emitting diode with external quantum efficiency over 20 %. *Angew. Chem. Int. Ed.* **62**, e202216473 (2023).
50. Yang, M., Park, I. S. & Yasuda, T. Full-color, narrowband, and high-efficiency electroluminescence from boron and carbazole embedded polycyclic heteroaromatics. *J. Am. Chem. Soc.* **142**, 19468–19472 (2020).
51. Hu, Y. et al. Narrowband fluorescent emitters based on BN-doped polycyclic aromatic hydrocarbons for efficient and stable organic light-emitting diodes. *Angew. Chem. Int. Ed.* **62**, e202312666 (2023).
52. Zou, Y. et al. High-performance narrowband pure-red OLEDs with external quantum efficiencies up to 36.1% and ultralow efficiency Roll-Off. *Adv. Mater.* **34**, 2201442 (2022).
53. Fan, T. et al. High-efficiency narrowband multi-resonance emitter fusing indolocarbazole donors for BT. 2020 red electroluminescence and ultralong operation lifetime. *Adv. Mater.* **35**, 2301018 (2023).
54. Jing, Y.-Y. et al. Precise modulation of multiple resonance emitters toward efficient electroluminescence with pure-red gamut for high-definition displays. *Sci. Adv.* **9**, eadh8296 (2023).
55. He, J. et al. Phenoxazine and phenothiazine embedded multi-resonance emitters for highly efficient pure-red OLEDs with improved color purity. *Chem. Eng. J.* **471**, 144565 (2023).
56. Miao, J. et al. Modulation of carbazole/phenol resonant partners within diboron-based multi-resonance emitters enable high-performance narrowband green to red OLEDs. *Adv. Funct. Mater.* **34**, 2316323 (2024).
57. Wang, Y. et al. Boron-, sulfur- and nitrogen-doped tridecacyclic aromatic emitters with multiple resonance effect for narrowband red emission†. *Chin. J. Chem.* **40**, 2671–2677 (2022).
58. Wang, H. et al. Efficient solution-processable OLEDs near BT.2020 red standard enabled by a multiresonant emitter. *Sci. Bull.* **69**, 2983–2986 (2024).
59. Hayakawa, M. et al. "Core-shell" wave function modulation in organic narrowband emitters. *J. Am. Chem. Soc.* **146**, 18331–18340 (2024).
60. Zou, Y. et al. Precisely regulating the double-boron-based multi-resonance framework towards pure-red emitters: high-performance OLEDs with CIE coordinates fully satisfying the BT. 2020 standard. *Mater. Horiz.* **10**, 3712–3718 (2023).
61. Yuan, L. et al. Color-tunable circularly polarized electroluminescence from a helical chiral multiple resonance emitter with B-N bonds. *Sci. China Chem.* **66**, 2612–2620 (2023).
62. Meng, G. et al. B-N covalent bond embedded double hetero-[n] helicenes for pure red narrowband circularly polarized electroluminescence with high efficiency and stability. *Adv. Mater.* **36**, 2307420 (2024).
63. Zhan g, Y. et al. Multi-resonance deep-red emitters with shallow potential-energy surfaces to surpass energy-gap law**. *Angew. Chem. Int. Ed.* **60**, 20498–20503 (2021).
64. Hua, T. et al. Narrowband near-infrared multiple-resonance thermally activated delayed fluorescence emitters towards high-performance and stable organic light-emitting diodes. *Angew. Chem. Int. Ed.* **63**, e202318433 (2024).
65. Yin, C. et al. Highly efficient and nearly roll-off–free electrofluorescent devices via multiple sensitizations. *Sci. Adv.* **8**, eabp9203 (2022).
66. Wang, H. et al. Stable and efficient phosphorescent organic light-emitting device utilizing a δ-carboline-containing host displaying thermally activated delayed fluorescence. *J. Mater. Chem. C.* **8**, 3800–3806 (2020).
67. Zhu, W. G. et al. Red electrophosphorescence of novel Ir-complexes in PLEDs. *Synth. Met* **137**, 1079–1080 (2003).
68. Uoyama, H. et al. Highly efficient organic light-emitting diodes from delayed fluorescence. *Nature* **492**, 234–238 (2012).
69. Wong, M. Y. & Zysman-Colman, E. Purely organic thermally activated delayed fluorescence materials for organic light-emitting diodes. *Adv. Mater.* **29**, 1605444 (2017).
70. Gottardi, S., Barbry, M., Coehoorn, R. & van Eersel, H. Efficiency loss processes in hyperfluorescent OLEDs: a kinetic Monte Carlo study. *Appl. Phys. Lett.* **114**, 073301 (2019).
71. Stavrou, K., Franca, L. G., Danos, A. & Monkman, A. P. Key requirements for ultraefficient sensitization in hyperfluorescence organic light-emitting diodes. *Nat. Photon* **18**, 554–561 (2024).
72. Cho, H.-H. et al. Suppression of Dexter transfer by covalent encapsulation for efficient matrix-free narrowband deep blue hyperfluorescent OLEDs. *Nat. Mater.* **23**, 519–526 (2024).
73. Frisch, M. J. et al. *Gaussian 16, Revision A.02*. https://gaussian.com/gaussian16/ (2016).

74. Ernzerhof, M. & Scuseria, G. E. Assessment of the perdew-burke-ernzerhof exchange-correlation functional. *J. Chem. Phys.* **110**, 5029–5036 (1999).
75. Adamo, C. & Barone, V. Toward reliable density functional methods without adjustable parameters: the PBE0 model. *J. Chem. Phys.* **110**, 6158–6169 (1999).
76. Perdew, J. P., Burke, K. & Ernzerhof, M. Generalized gradient approximation made simple. *Phys. Rev. Lett.* **77**, 3865–3868 (1996).
77. Perdew, J. P., Burke, K. & Ernzerhof, M. Errata: Generalized gradient approximation made simple. *Phys. Rev. Lett.* **78**, 1396 (1997).
78. Peng, Q. et al. Correlation function formalism for triplet excited state decay: combined spin–orbit and nonadiabatic couplings. *J. Chem. Theory Comput* **9**, 1132–1143 (2013).
79. Niu, Y. et al. MOlecular materials property prediction package (MOMAP) 1.0: a software package for predicting the luminescent properties and mobility of organic functional materials. *Mol. Phys.* **116**, 1078–1090 (2018).
80. Niu, Y., Peng, Q. & Shuai, Z. Promoting-mode free formalism for excited state radiationless decay process with Duschinsky rotation effect. *Sci. China Ser. B Chem.* **51**, 1153–1158 (2008).
81. Peng, Q., Yi, Y., Shuai, Z. & Shao, J. Toward quantitative prediction of molecular fluorescence quantum efficiency: role of Duschinsky rotation. *J. Am. Chem. Soc.* **129**, 9333–9339 (2007).
82. Lu, T. & Chen, F. Multiwfn: a multifunctional wavefunction analyzer. *J. Comput. Chem.* **33**, 580–592 (2012).
83. Neese, F. The ORCA program system. *WIREs Comput. Mol. Sci.* **2**, 73–78 (2012).
84. Neese, F. Software update: the ORCA program system, version 4.0. *WIREs Comput. Mol. Sci.* **8**, e1327 (2018).
85. Neese, F. et al. The ORCA quantum chemistry program package. *J. Chem. Phys.* **152**, 224108 (2020).

Acknowledgements

This work was supported by the Jilin Provincial Science and Technology Development Plan Project (SKL202402010), Young Scientists Fund of the NSFC (Grant No. 52203230), National Natural Science Foundation of China (21935005 and 52173165), the National Key R&D Program of China (2020YFA0714601), Natural Science Foundation of Chongqing, China (cstc2021jcyj-msxmX0274) and Open Fund of the Key Lab of Organic Optoelectronics and Molecular Engineering of Ministry of Education (53223000122), Young Elite Scientists Sponsorship Program by CAST (Grant No. 2022QNRC001).

Author contributions

Y.W. and L.D. conceived the project. Y.W.Z., C.L.L., L.D., and Y.W. supervised the project. Y.X.P., Y.W.Z., and C.L.L. analyzed the data and wrote the manuscript. Y.X.P. synthesized the emitters. Y.X.P., Y.W.Z., and C.L.L. characterized the emitters and gauged the photophysical and electrochemical properties. Y.X.P. fabricated and evaluated the OLEDs. Q.J. executed theoretical computations; L.D. and Y.W. reviewed and edited the manuscript. All authors deliberated on the advancement of the research and scrutinized the manuscript.

Competing interests

The authors declare no competing interests.

Additional information

Supplementary information The online version contains supplementary material available at https://doi.org/10.1038/s41467-024-55680-2.

Correspondence and requests for materials should be addressed to Yuewei Zhang, Chenglong Li, Lian Duan or Yue Wang.

Peer review information *Nature Communications* thanks Piotr Pander, and the other, anonymous, reviewer(s) for their contribution to the peer review of this work. A peer review file is available.